

# DD3IMP, 3D FULLY IMPLICIT FINITE ELEMENT SOLVER: IMPLEMENTATION OF CB2001 YIELD CRITERION

P.D. BARROS<sup>1</sup>, D.M. NETO<sup>1</sup>, J.L. ALVES<sup>2</sup>, M.C. OLIVEIRA<sup>1</sup>, L.F. MENEZES<sup>1</sup>

*Abstract.* The strategies and algorithms adopted in the fully implicit FE solver DD3IMP to model the orthotropic behavior of metallic sheets, as well the procedure for parameters' identification, are the main focus of this work; a special and detailed emphasis will be given to the numerical implementation of the Cazacu and Barlat (2001) yield criterion. The usage and application of the aforesaid solver and yield criterion will be exemplified with the deep drawing of a cylindrical cup, an example typically adopted to study the effect of the material's orthotropy in forming operations. Two materials with distinct anisotropic behaviors are considered, namely: the AA5042 aluminum alloy and the AKDQ steel. The material parameters are identified from experimental data taking into account both flow stresses and  $r$ -values. The analysis of the results indicates that a good description of the anisotropy of both flow stresses and  $r$ -values are important to the overall accuracy of the predicted earing profile. However, either the global process history or the process parameters may influence the earing prediction, particularly the contact interactions with the flange during the forming process.

*Key words:* DD3IMP, implicit time integration, sheet metal forming, elastoplasticity, orthotropy, CB2001 yield criterion.

## 1. INTRODUCTION

Nowadays, the virtual try-out of sheet metal forming components has become an indispensable tool for the automotive industry, providing a strong reduction of development times. The process parameters optimization can be performed by a computer system in a virtual environment, replacing the expensive trial-and-error procedures by numerical ones [1]. Despite recent developments in the numerical tools, the finite element analysis of sheet metal forming processes still represents a challenge from the computational and modelling point of view; the problem is

---

<sup>1</sup> CEMUC, Department of Mechanical Engineering, University of Coimbra, Polo II, Pinhal de Marrocos, 3030-788 Coimbra, Portugal

<sup>2</sup> MEMS, Microelectromechanical Systems Research Unit, University of Minho, Campus de Azurém, 4800-058 Guimarães, Portugal

highly nonlinear due to the large deformations (geometry), the elastoplastic behavior (material) and the occurrence of frictional contact between the blank and the forming tools. Therefore, effective and robust finite element algorithms are required to provide accurate predictions when dealing with such complex industrial problems.

The time integration scheme used in the problem formulation dictates the efficiency and robustness of numerical simulations [2]. The dynamic explicit and the static implicit procedures are the two main formulations currently adopted [3]. Historically, the sheet metal forming analysis has been mainly carried out using explicit time integration schemes, which do not require an iterative procedure in each time increment, and thus avoiding convergence problems. Nevertheless, this method is only conditionally stable, requiring extremely small time steps (smaller than a critical time step) to guarantee the stability of the numerical solution. Thus, for *quasi*-static processes like typical sheet metal forming operations, when using dynamic explicit schemes it is necessary to resort to artificial strategies such as higher tool velocities to artificially increase the time step and achieve admissible computational times. Besides, in opposition to the static implicit schemes, the explicit procedures do not check equilibrium requirements at the end of each time increment [4]. Therefore, particularly when analyzing the influence of constitutive models in the numerical results accuracy, it is consensual that implicit time integration schemes lead to more accurate results (see e.g. [5]).

The elastoplastic behavior of the metallic sheet, namely the anisotropy and the work-hardening, are usually described by phenomenological constitutive models, which have a strong impact in the numerical solutions [6]. The material's orthotropic behavior is modelled by the yield surface, used to describe the yielding and the plastic flow of the material: this dual role of the yield surface requires a particular care and accuracy in its modeling and numerical implementation. Also, due to the increasingly advanced materials, the yield surface modeling has become more complex, relying on an increasing number of material parameters. However, some authors point out that although they are capable of a more accurate description of the in-plane directional (uniaxial) properties, they may predict sensibly different plastic properties for neighboring stress states.

The aim of this work is to present the algorithm adopted in the implementation of the non-quadratic yield criterion proposed by Cazacu and Barlat (2001) [7] in the implicit in-house code DD3IMP, and the strategies for parameters identification. The case study selected for analysis is a cylindrical cup deep drawing, since it is one of the typical forming operations in which the effect of the material's orthotropic behavior is more pronounced. Since the numerical results are also influenced by other numerical aspects, such as the finite elements adopted and the algorithm for contact with friction treatment, a brief description of the state update algorithm of DD3IMP is presented in the next section.

## 2. DD3IMP FINITE ELEMENT SOLVER

A brief description of the mechanical model and numerical methods currently implemented in the FE solver DD3IMP, which has been continuously developed and optimized to simulate sheet metal forming processes [8, 9], is given in this section. The evolution of the deformation process is described by an updated Lagrangian scheme. The mechanical model takes into account the large elastoplastic deformations and rotations of the deformable body (metallic sheet). Besides, the hypothesis of small elastic strains is adopted, assuming that the elastic strains are negligibly small with respect to unity. The forming tools are assumed as rigid bodies, while the frictional contact between the sheet and the tools is described by the Coulomb's classical law. The augmented Lagrangian approach proposed by Alart and Curnier [10] is used to regularize the constraints arising from the frictional contact conditions. Both nodal displacements and contact forces are involved in the resulting system of nonlinear equations, leading to a mixed formulation. A fully implicit Newton–Raphson method is adopted to solve, in a single iterative loop, all problem nonlinearities (geometry, material and contact) [8].

In order to improve the convergence rate of the numerical simulation, each time increment is divided into two steps: (i) the *Predictor* step, which determines the explicit trial solution, and (ii) the *Corrector* step, where this solution is iteratively corrected by an implicit method. Since the quality of the trial solution provided by the *Predictor* step is determinant for the convergence of the iterative process, a  $r_{\min}$  strategy is employed to impose several restrictions and optimize the time step size [11]. Then, the equilibrium state of the deformable body is satisfied in each time step using the Newton-Raphson algorithm, which exhibits quadratic convergence in the vicinity of the solution (equilibrium).

The forming tools are modelled with Nagata patches [12], which result from the surface smoothing procedure applied to a coarse mesh [13]. The blank sheet is discretized with 3D solid finite elements, allowing an accurate evaluation of the contact forces and the stress gradients through the thickness [14]. Since the equilibrium conditions are checked in each time step, the use of solid elements is more CPU time consuming. Therefore, some high performance computing techniques have been incorporated, such as OpenMP directives, in the most time consuming branches of the code [15].

The elastoplastic constitutive model adopted considers isotropic elasticity and anisotropic plasticity. The elastic regime is described by the generalized Hooke law, while the plastic behavior of the material is modelled by: (i) an associated flow rule; (ii) a yield criterion and (iii) a work-hardening law. Several yield criteria are currently implemented, namely: (i) Hill'48 [16]; (ii) Barlat'91 [17]; (iii) Drucker [18]; (iv) Karafillis & Boyce'93 [19]; (v) Cazacu & Barlat'01 [7] and Cazacu, Plunkett & Barlat'06 [20]. Concerning the work-hardening law, which describes the evolution of the yield surface with the plastic work, various laws are available:

(i) pure isotropic hardening by means of a power law (Swift) or a Voce type saturation law; (ii) the combination of these two laws with a linear (Prager type) or non-linear kinematic hardening law proposed by Lemaître and Chaboche [21]; and (iii) the microstructural hardening model proposed by Teodosiu and Hu [22].

## 2.1. THE CONSTITUTIVE MODEL

The differential form of the elastoplastic behavior law is, in its general form,

$$\dot{\boldsymbol{\sigma}}^J = \mathbf{C}^{\text{ep}} : \mathbf{D}, \quad (1)$$

where  $\dot{\boldsymbol{\sigma}}^J$  is the Jaumann derivative of the Cauchy stress tensor  $\boldsymbol{\sigma}$ , given by

$$\dot{\boldsymbol{\sigma}}^J = \dot{\boldsymbol{\sigma}} + \boldsymbol{\sigma}\mathbf{W} - \mathbf{W}\boldsymbol{\sigma}, \quad (2)$$

where  $\dot{\boldsymbol{\sigma}}$  stands for the time derivative of the Cauchy stress tensor and  $\mathbf{W}$  is the total spin tensor defined by

$$\mathbf{W} = \dot{\mathbf{R}}\mathbf{R}^T, \quad (3)$$

with  $\mathbf{R}$  being the orthogonal elastic rotation tensor.  $\mathbf{D}$  is the strain rate tensor and  $\mathbf{C}^{\text{ep}}$  is a fourth-order tensor corresponding to the elastoplastic module. This tensor depends of the algorithms adopted in the integration of the constitutive model and the type of relation considered between the states at the beginning and at the end of the loading increment. Thus, it is possible to consider the tangent elastoplastic modulus or the consistent elastoplastic modulus. The tangent elastoplastic modulus can be defined as [23]

$$\mathbf{C}^{\text{ep}} \Big|_{\text{tangent}} = \mathbf{C}^e - \alpha f_0 \mathbf{V} \otimes \mathbf{V}, \quad (4)$$

where  $\alpha = 0$  if the material is in an elastic state, or during elastic unloading; and  $\alpha = 1$  if the material is in an elastoplastic loading state.  $f_0$  is a function of the isotropic and kinematic hardening law adopted. Although the example considered in this work does not include kinematic hardening, in order to keep the back-stress tensor in the equations, the Prager's kinematic law,  $\dot{\mathbf{X}} = k\mathbf{D}^p$ , is considered, with the single parameter  $k$ . Therefore,  $f_0$  can be written in the general form

$$f_0 = \frac{4\mu^2}{(k + 2\mu)\mathbf{V} : \mathbf{V} + H'}, \quad (5)$$

where  $\mu$  is the Lamé parameter.  $\mathbf{V}$  is one of the tensorial quantities to be determined as function of the adopted yield criterion, and it is, by definition

$$\mathbf{V} = \frac{\partial \bar{\sigma}}{\partial (\boldsymbol{\sigma}' - \mathbf{X})}, \quad (6)$$

where  $\bar{\sigma}$  is the equivalent stress given by the yield criterion,  $\boldsymbol{\sigma}'$  the deviatoric Cauchy stress tensor, and  $\mathbf{X}$  the deviatoric and symmetric second-order back-stress tensor.

The strain rate can be decomposed into elastic and plastic parts as

$$\mathbf{D} = \mathbf{D}^e + \mathbf{D}^p, \quad (7)$$

where  $\mathbf{D}^p$ , the plastic strain rate tensor, is a deviatoric tensor, given by the associated inviscid flow rule as

$$\mathbf{D}^p = \dot{\lambda} \frac{\partial \mathcal{F}}{\partial (\boldsymbol{\sigma}' - \mathbf{X})} = \dot{\lambda} \mathbf{V}, \quad (8)$$

in which  $\dot{\lambda}$  is the plastic multiplier and  $\mathcal{F}$  is the plastic potential, identified as a scalar function defining the elastic limit surface, such that

$$\mathcal{F}(\bar{\sigma}, Y) = \bar{\sigma} - Y = 0, \quad (9)$$

where  $Y$  is the flow stress, modelled by the isotropic work-hardening law. From this definition, the consistency condition in rate form states that

$$\dot{\mathcal{F}}(\bar{\sigma}, Y) = \dot{\bar{\sigma}} - H' \dot{\bar{\epsilon}}^p = 0, \quad (10)$$

where

$$H' = \partial Y / \partial \bar{\epsilon}^p \quad (11)$$

is the isotropic hardening modulus, and, if the yield function is a homogeneous function of degree one, one has that  $\dot{\bar{\epsilon}}^p = \dot{\lambda} \cdot \dot{\bar{\sigma}}$  and  $\dot{\bar{\epsilon}}^p$  are, respectively, the time derivatives of the equivalent stress and of the equivalent plastic strain. The total equivalent plastic strain is defined as

$$\bar{\epsilon}^p = \int_0^t \frac{(\boldsymbol{\sigma}' - \mathbf{X}) : \mathbf{D}^p}{\bar{\sigma}} dt. \quad (12)$$

## 2.2. TIME INTEGRATION

Since the elastic behavior is considered isotropic, the hypoelastic form of the Hooke's law can be written as [23]

$$\dot{\boldsymbol{\sigma}} = \mathbf{C}^e : (\mathbf{D} - \mathbf{D}^p) \quad (13)$$

which, by integration, corresponds to the stress increment in  $[t, t + \Delta t]$ , i.e.

$$\boldsymbol{\sigma}_F - \boldsymbol{\sigma}_0 = \mathbf{C}^e : \Delta \boldsymbol{\varepsilon} - \mathbf{C}^e : \Delta \boldsymbol{\varepsilon}^p \quad (14)$$

with subscripts 0 and F denoting the quantities at the beginning and at the end of the time increment  $[t, t + \Delta t]$ , respectively.  $\Delta \boldsymbol{\varepsilon}^p$  and  $\Delta \boldsymbol{\varepsilon}$  are the increments of the plastic and total strain tensors, respectively, determined over the time increment. Applying the generalized middle point rule to determine the  $\mathbf{D}^p$  evolution, and since  $\mathbf{D}^p = \dot{\lambda} \mathbf{V}$ , it can be written

$$\Delta \boldsymbol{\varepsilon}^p = \Delta \lambda \mathbf{V}_\gamma, \quad (15)$$

with

$$\mathbf{V}_\gamma = (1 - \gamma) \mathbf{V}_0 + \gamma \mathbf{V}_F \quad \text{and} \quad \gamma \in [0, 1]. \quad (16)$$

To calculate  $\Delta \lambda$  and  $\mathbf{V}_F$  it is necessary to determine  $(\boldsymbol{\sigma}'_F - \mathbf{X}_F)$ .  $\boldsymbol{\sigma}'_F$  is calculated from Eq. 14, leading to deviatoric and hydrostatic components given by, respectively,

$$\boldsymbol{\sigma}'_F = \boldsymbol{\sigma}'_0 + 2G\Delta \boldsymbol{\varepsilon}' - 2G\Delta \lambda \mathbf{V}_F \quad \text{and} \quad (17)$$

$$\text{tr}(\boldsymbol{\sigma}'_F) = \text{tr}(\boldsymbol{\sigma}'_0) + \frac{E}{1 + 2\nu} \text{tr}(\Delta \boldsymbol{\varepsilon}). \quad (18)$$

$G$  and  $E$  are the shear and Young's modulus, while  $\nu$  is the Poisson's ratio. In order to determine both  $(\boldsymbol{\sigma}'_F - \mathbf{X}_F)$  and  $\Delta \bar{\varepsilon}^p = \Delta \lambda$ , the consistency condition at the end of the time step is imposed, i.e.,

$$\bar{\sigma}(\boldsymbol{\sigma}'_F - \mathbf{X}) - Y_F (\bar{\varepsilon}_0^p + \Delta \bar{\varepsilon}^p) = 0. \quad (19)$$

This allows to define the non-linear system of equations to be solved in the state update algorithm, with unknowns  $(\boldsymbol{\sigma}'_F - \mathbf{X}_F)$  and  $\Delta \bar{\varepsilon}^p$ , i.e.,

$$\mathcal{Q}(\boldsymbol{\sigma}'_F - \mathbf{X}_F, \Delta \bar{\varepsilon}^p) = \begin{bmatrix} \mathcal{G} \\ g \end{bmatrix} = \begin{bmatrix} \mathbf{0} \\ 0 \end{bmatrix}. \quad (20)$$

Assuming that the Prager's kinematic law is considered, the system of equations defined in Eq. 20 can be re-written as

$$\begin{bmatrix} (\boldsymbol{\sigma}'_F - \mathbf{X}_F) - (\boldsymbol{\sigma}'_0 - \mathbf{X}_0) - 2G\Delta \boldsymbol{\varepsilon}' - (k + 2G)\Delta \bar{\varepsilon}^p \mathbf{V}_F \\ \bar{\sigma}(\boldsymbol{\sigma}'_F - \mathbf{X}_F) - Y_F (\bar{\varepsilon}_0^p - \Delta \bar{\varepsilon}^p) \end{bmatrix} = \begin{bmatrix} \mathbf{0} \\ 0 \end{bmatrix}. \quad (21)$$

The updated state variables are determined solving the non-linear system of equations Eq. 21 using the Newton-Raphson method. The calculation of  $\mathcal{Q}$  and  $\partial\mathcal{Q}/\partial\boldsymbol{\varsigma}$  (with  $\boldsymbol{\varsigma} = [\boldsymbol{\sigma}'_F - \mathbf{X}_F, \Delta\bar{\varepsilon}^p]$ ) depends on the adopted yield criterion: the following matrix quantities must be analytically determined:

$$\frac{\partial\mathcal{Q}}{\partial\boldsymbol{\varsigma}} = \begin{bmatrix} [\mathbf{A}] & [\mathbf{c}] \\ [\mathbf{b}] & d \end{bmatrix}, \quad (22)$$

where

$$\mathbf{A} = \frac{\partial\mathcal{Q}}{\partial(\boldsymbol{\sigma}'_F - \mathbf{X}_F)}, \quad \mathbf{b} = \frac{\partial g}{\partial(\boldsymbol{\sigma}'_F - \mathbf{X}_F)}, \quad \mathbf{c} = \frac{\partial\mathcal{G}}{\partial(\Delta\bar{\varepsilon}^p)}, \quad d = \frac{\partial g}{\partial(\Delta\bar{\varepsilon}^p)}. \quad (23)$$

In the case of Prager's kinematic hardening law, these expression can be written as:

$$\mathbf{A} = \mathbf{I}_4 + (k + 2G)\Delta\bar{\varepsilon}^p\mathbf{Q}_F, \quad \mathbf{c} = \mathbf{V}_F, \quad (24)$$

$$\mathbf{b} = \mathbf{V}_F, \quad d = -H'_F,$$

where

$$\mathbf{V}_F = \frac{\partial\bar{\sigma}}{\partial(\boldsymbol{\sigma}'_F - \mathbf{X}_F)}, \quad \mathbf{Q}_F = \frac{\partial^2\bar{\sigma}}{\partial(\boldsymbol{\sigma}'_F - \mathbf{X}_F)^2} \quad \text{and} \quad H'_F = \partial Y / \partial\bar{\varepsilon}^p. \quad (25)$$

The tensor  $\mathbf{Q}$  corresponds to the second order derivative of the yield criterion with respect to the effective stress state  $\boldsymbol{\Sigma} = \boldsymbol{\sigma}' - \mathbf{X}$ , being used both in the state update algorithm and on the definition of the consistent elastoplastic modulus,

$$\mathbf{C}^{ep} = \mathbf{C}^e - 4G^2(1-\beta) \left( \frac{\mathbf{V}_F \otimes \mathbf{V}_F}{H'_F} + \Delta\bar{\varepsilon}^p\mathbf{Q}_F \right) \boldsymbol{\Lambda}, \quad (26)$$

where  $\boldsymbol{\Lambda}$  also depends on the kinematic hardening law adopted. In case of Prager's kinematic hardening law it can be written as

$$\boldsymbol{\Lambda}^{-1} = \left[ \mathbf{I}_4 + (k + 2\mu) \left( \frac{\mathbf{V}_F \otimes \mathbf{V}_F}{H'_F} + \Delta\bar{\varepsilon}^p\mathbf{Q}_F \right) \right]. \quad (27)$$

Since the strain increment can be either elastic or plastic, parameter  $\beta$  and  $(1-\beta)$  is introduced in Eq. 26 to separate, respectively, the elastic and plastic parts of the total strain increment.

### 2.3. CAZACU AND BARLAT YIELD CRITERION

The Cazacu and Barlat (2001) [7] yield criterion is a generalization of the Drucker's isotropic criterion to orthotropy, and, in its general form, is given by:

$$\bar{\sigma} = \left\{ 27 \left[ \left( J_2^0 \right)^3 - c \left( J_3^0 \right)^2 \right] \right\}^{\frac{1}{6}}, \quad (28)$$

where  $J_2^0$  and  $J_3^0$  are the second and third generalized invariants of the effective stress tensor  $\Sigma$ , defined as

$$\begin{aligned} J_2^0 &= \frac{a_1}{6} (\Sigma_{11} - \Sigma_{22})^2 + \frac{a_2}{6} (\Sigma_{11} - \Sigma_{33})^2 + \frac{a_3}{6} (\Sigma_{22} - \Sigma_{33})^2 \\ &\quad + a_4 \Sigma_{12}^2 + a_5 \Sigma_{13}^2 + a_6 \Sigma_{23}^2, \quad (29) \\ J_3^0 &= (1/27)(b_1 + b_2) \Sigma_{11}^3 + (1/27)(b_3 + b_4) \Sigma_{22}^3 \\ &\quad + (1/27)[2(b_1 + b_4) - b_2 - b_3] \Sigma_{33}^3 \\ &\quad - (1/9)(b_1 \Sigma_{22} + b_2 \Sigma_{33}) \Sigma_{11}^2 - (1/9)(b_3 \Sigma_{33} + b_4 \Sigma_{11}) \Sigma_{22}^2 \\ &\quad - (1/9)[(b_1 - b_2 + b_4) \Sigma_{11} + (b_1 - b_3 + b_4) \Sigma_{22}] \Sigma_{33}^2 \\ &\quad + (2/9)(b_1 + b_4) \Sigma_{11} \Sigma_{22} \Sigma_{33} \\ &\quad - (\Sigma_{13}^2/3)[2b_9 \Sigma_{22} - b_8 \Sigma_{33} - (2b_9 - b_8) \Sigma_{11}] \\ &\quad - (\Sigma_{12}^2/3)[2b_{10} \Sigma_{33} - b_5 \Sigma_{22} - (2b_{10} - b_5) \Sigma_{11}] \\ &\quad - (\Sigma_{23}^2/3)[(b_6 - b_7) \Sigma_{11} - b_6 \Sigma_{22} - b_7 \Sigma_{33}] + 2b_{11} \Sigma_{12} \Sigma_{23} \Sigma_{13}, \quad (30) \end{aligned}$$

where  $c$ ,  $a_1, \dots, a_6$  and  $b_1, \dots, b_{11}$  are the anisotropy parameters.  $\Sigma_{ij}$ ,  $i, j = 1, 2, 3$  are the effective stress components defined in the material frame. For metal sheets, parameters  $a_5$ ,  $a_6$  and  $b_k$  ( $k = 6, 7, 8, 9, 11$ ) cannot be evaluated, thus the corresponding commonly isotropic values are adopted, i.e. 1.0. Although the anisotropy parameters reduce from 18 to 11, this yield function is flexible enough to enable the accurate description of the in-plane anisotropy of both  $r$ -value and flow stresses (or yield stresses).

The analytical expressions for the tensorial quantities  $\mathbf{V}$  and  $\mathbf{Q}$ , previously introduced in Eq. 24, are detailed in Appendix A in case of CB2001 yield criterion, along with the definition of the scalar quantity  $\beta$  (see Eq. 26).

### 3. DEEP DRAWING AND IRONING OF A CYLINDRICAL CUP

The deep-drawing of an axisymmetric cylindrical cup, benchmark proposed in the framework of Numisheet 2011 conference [24], was the example selected in this work to highlight the overall performance and capabilities of DD3IMP. This example encompasses two forming stages: (i) deep-drawing and (ii) ironing of the cylindrical cup. The geometry of the forming tools for both operations is shown in Fig. 1 (a). The specific geometry of the die allows to perform both the drawing and the ironing operations within one punch stroke. Therefore, the process is modeled considering three phases: (i) closing of the blank-holder until attain a prescribed force of 8.9 kN; (ii) punch displacement of 72.1 mm and (iii) springback. Due to geometrical and material symmetries, only one quarter of the global structure is modeled. The radius of the blank sheet is 38.062 mm for both materials (AA5042 aluminum alloy and AKDQ steel). The initial thickness of the blank is 0.208 mm for the AA5042 aluminum and 0.229 mm for the AKDQ steel. The blank sheet was discretized with 8-node hexahedral finite elements, combined with a selective reduced integration technique [25]. The use of solid finite elements is particularly important to simulate the ironing phase, due to double sided contact. Fig. 1 (b) presents the in-plane finite element mesh considered in the analysis. This mesh was built considering two layers of elements through thickness, leading to a total of 8464 finite elements [26]. The friction coefficient between the blank and the (rigid) forming tools is considered as  $\mu=0.05$ , according with the benchmark description [24]. All simulations were carried out in a single multi-core CPU workstation: Intel® Core™ i7-2600K (3.4 GHz) CPU and the Windows7 Professional (64-bits platform) operating system.

The materials' mechanical behavior is assumed isotropic in the elastic regime, being described by the Young's modulus,  $E$ , and the Poisson ratio,  $\nu$ . The plastic behavior is described using an isotropic work hardening Voce type law,

$$Y(\bar{\epsilon}^p) = Y_0 + (Y_{\text{sat}} - Y_0) \left[ 1 - \exp(-C_Y \bar{\epsilon}^p) \right], \quad (31)$$

where  $Y_0$ ,  $Y_{\text{sat}}$  and  $C_Y$  are material parameters. The parameters assumed for the isotropic work hardening law adopted for both materials correspond to the ones identified by the benchmark committee for the tensile test performed along the rolling direction (Table 1).

Besides the CB2001 yield criterion, also the well-known Hill'48 yield criterion was considered and used as reference for comparison purposes and analysis. In this case, the equivalent stress is defined as

$$\begin{aligned} \bar{\sigma}^2 = & F(\Sigma_{22} - \Sigma_{33})^2 + G(\Sigma_{33} - \Sigma_{11})^2 + H(\Sigma_{11} - \Sigma_{22})^2 \\ & + 2L\Sigma_{23}^2 + 2M\Sigma_{13}^2 + 2N\Sigma_{12}^2, \end{aligned} \quad (32)$$

where  $F$ ,  $G$ ,  $H$ ,  $L$ ,  $M$  and  $N$  are the anisotropy parameters. For thin metallic sheets, it is not possible to determine parameters  $L$  and  $M$ . Therefore, the values considered for these parameters are the ones corresponding to the isotropic case, i.e. 1.5.

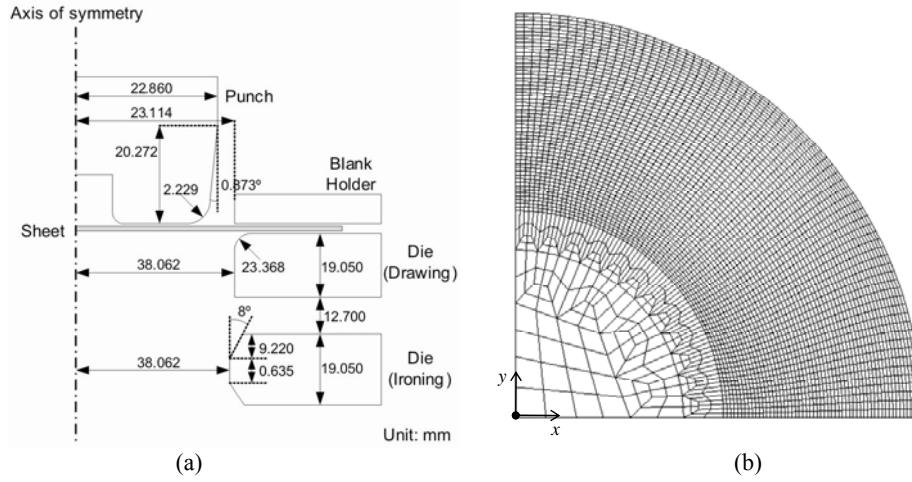


Fig. 1 – Forming tools and blank geometry: a) main dimensions; b) in-plane blank sheet discretization.

Table 1

Elastic and work hardening properties for both materials

		AA5042	AKDQ
Elastic properties	$E$ [GPa]	68.9	210.0
	$\nu$	0.33	0.30
Voce law	$Y_0$ [MPa]	267.80	297.79
	$Y_{sat}$ [MPa]	375.08	471.76
	$C_Y$	17.859	15.889

The anisotropy parameters for both yield criteria were determined using the DD3MAT in-house code [27], taking into account the experimental data reported by the benchmark committee for uniaxial tensile, equi-biaxial tension and the disc compression tests [24]. In DD3MAT, the identification procedure adopted is based on the minimization of an error function that evaluates the differences between the estimated values and the experimental ones, as follows

$$F(\mathbf{A}) = \sum_{\theta=0}^{90} w_{\sigma_{\theta}^T} \left( \sigma_{\theta}^T(\mathbf{A}) / \sigma_{\theta}^T - 1 \right)^2 + \sum_{\theta=0}^{90} w_{r_{\theta}} \left( r_{\theta}(\mathbf{A}) / r_{\theta} - 1 \right)^2 + w_{\sigma_b} \left( \sigma_b(\mathbf{A}) / \sigma_b - 1 \right)^2 + w_{r_b} \left( r_b(\mathbf{A}) / r_b - 1 \right)^2, \quad (33)$$

where  $\mathbf{A}$  represents the set of parameters associated with the selected yield criterion,  $\sigma_{\theta}^T$  and  $r_{\theta}$  are the experimental yield stresses in tension and  $r$ -values, respectively, obtained from the uniaxial tensile tests for a specific orientation ( $\theta$ ) with respect to the rolling direction (RD).  $\sigma_b$  is the experimental yield stress obtained from the equibiaxial tensile test,  $r_b$  is the experimental  $r$ -value obtained from the disc compression test, and  $\sigma_{\theta}^T(\mathbf{A})$ ,  $r_{\theta}(\mathbf{A})$ ,  $\sigma_b(\mathbf{A})$  and  $r_b(\mathbf{A})$  are the correspondent values predicted from the adopted yield criterion. Such procedure can be considered a generalization of the one proposed by Banabic et al., 2005 [28], where the weighting factors,  $w_{\sigma_{\theta}^T}$ ,  $w_{r_{\theta}}$ ,  $w_{\sigma_b}$  and  $w_{r_b}$  are used to balance the influence of the experimental data. Nevertheless, the selection of the weighting factors is normally a manual procedure, strongly dependent on users' expertise and knowledge. In this study, all the weighting factors are considered equal to 1.0.

The parameters identification procedure takes into account, for both yield criteria, the yield stresses and  $r$ -values for 7 orientations to RD, the  $r_b$  value and the biaxial yield stress,  $\sigma_b$  (a total of 16 values). This results in an over constrained problem for both yield criteria, since the Hill'48 has only 4 parameters to be identified and CB2001 has 11. Nevertheless, recent studies indicate that the accurate prediction of the earing profile requires an accurate fit of the in-plane  $r$ -values anisotropy, but also of the yield stresses. Moreover, rather than capture values for specific orientations, it seems to be more relevant to be able to describe the trend of the anisotropy of the in-plane yield stresses [29]. For each orientation to the rolling direction  $\theta_i \in ]0^{\circ}, 90^{\circ}[$ , two auxiliary vectors are defined:

$$\mathbf{v}_{\theta_i}^{\text{exp}} = \begin{Bmatrix} \theta_{i+1} - \theta_{i-1} \\ \sigma_{\theta_{i+1}}^{\text{exp}} - \sigma_{\theta_{i-1}}^{\text{exp}} \end{Bmatrix} \quad \text{and} \quad \mathbf{v}_{\theta_i} = \begin{Bmatrix} \theta_{i+1} - \theta_{i-1} \\ \sigma_{\theta_{i+1}} - \sigma_{\theta_{i-1}} \end{Bmatrix}, \quad (34)$$

using the experimental and the numerical yield stress values, respectively. This enables the evaluation of the trend error for each angle  $\theta_i$ , using the dot product between both vectors (i.e. the trend is the same for a value of  $\mathbf{v}_{\theta_i}^{\text{exp}} \cdot \mathbf{v}_{\theta_i}$  equal to 1.0). In order to integrate the two objectives in the optimization problem, a new objective function was added to the one defined in Eq. 33, in order to avoid the use of multi-objective optimization algorithms. The new objective function adds the difference in the yield stress trend, between two consecutive orientations, being defined as:

$$F_{\text{trend}}(\mathbf{A}) = F(\mathbf{A}) + w_{\text{trend}} \sum_{\theta=0}^{90} \left( 1 - \left( \frac{\mathbf{v}_{\theta_i}^{\text{exp}} \cdot \mathbf{v}_{\theta_i}}{\|\mathbf{v}_{\theta_i}^{\text{exp}}\| \|\mathbf{v}_{\theta_i}\|} \right) \right). \quad (35)$$

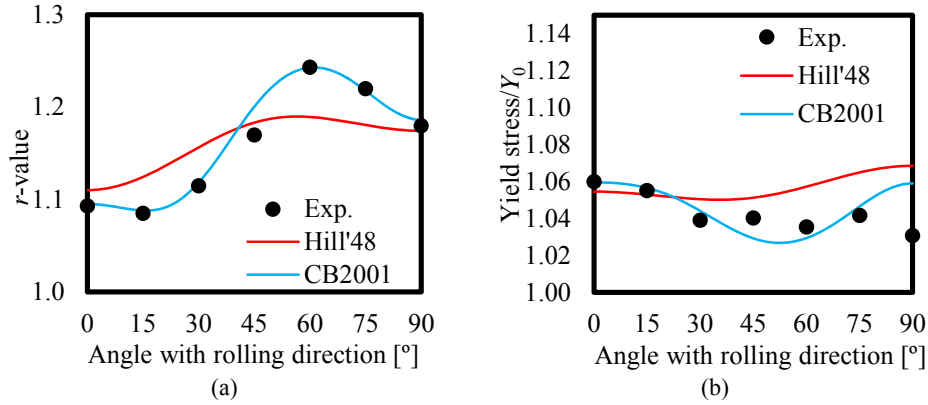
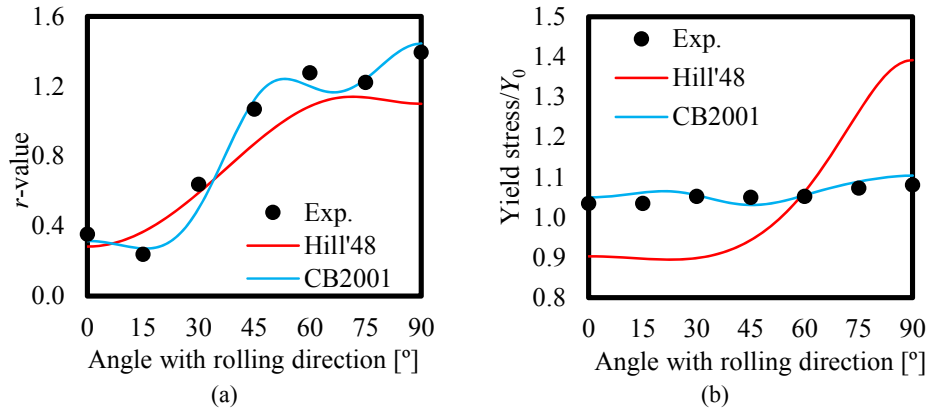
$w_{\text{trend}}$  corresponds to the weight given to the function that tries to improve the correlation between the experimental and the predicted trend for the in-plane yield stresses directionalities. As for the weight used in function  $F(\mathbf{A})$ , the selection of this weighting factor is also a manual procedure. Another comment should be added concerning the fact that the conditions that guarantee the convexity of CB2001 are unknown. Therefore, following Soare *et al.* [30], the minimization process adopted for this yield criterion includes testing the convexity of the yield surface, for several planes in the stress space [31]. The algorithm implemented in DD3MAT to minimize the cost function is based on a downhill simplex method.

Table 2 presents a summary of the parameters determined for both yield criteria and both materials, using the optimization procedure previously described.  $w_{\text{trend}}$  was considered null except in case of the identification of the aluminum alloy and CB2001 yield criterion. Besides, the Hill'48 yield criterion is not flexible enough to enable an accurate description of the anisotropy of both  $r$ -values and yield stresses. Moreover, the inclusion of the new objective functions tends to penalize the accuracy of the  $r$ -values anisotropy.

Table 2

Identified parameters for both materials (AA5042 and AKDQ) and yield criteria (Hill'48 and CB2001)

		AA5042	AKDQ
Hill'48	$F$	0.2457	0.4028
	$G$	0.9553	0.4261
	$H$	0.2704	0.4730
	$N$	1.6459	1.3951
	$L = M$	1.5000	1.5000
CB2001	$a_1$	0.9425	1.0462
	$a_2$	0.6986	0.9568
	$a_3$	1.0778	0.9681
	$a_4$	0.9792	1.0599
	$b_1$	6.0000	1.1731
	$b_2$	-0.3273	1.1183
	$b_3$	2.8941	1.1681
	$b_4$	-2.5143	1.0252
	$b_5$	-2.4348	0.8815
	$b_{10}$	1.2299	1.0622
	$c$	0.2397	1.6209

Fig. 2 – Experimental and predicted: a) *r*-values; b) yield stresses for AKDQ.Fig. 3 – Experimental and predicted: a) *r*-values; b) yield stresses for AA5042.

Figures 2 and 3 present the comparison between the numerical and experimental *r*-values and the normalized yield stresses, for the AKDQ steel and AA5042 aluminum, respectively. The tensile yield stresses are normalized with the yield stress predicted by the hardening law, i.e.  $Y_0$ , which is different from the value reported for  $\sigma_0^T$  (see [24]). The AKDQ steel presents an almost isotropic distribution of the in-plane *r*-values and yield stresses. The CB2001 yield criterion, as expected, allows a better description of both yield stress directionalities and *r*-values. The AA5042 aluminum alloy presents a strong anisotropy of the *r*-values, while being almost isotropic in the tensile yield stresses. Therefore, the Hill'48 only captures the proper trend for the *r*-values. The CB2001 yield criterion allows the description of the anisotropy of both yield stresses and *r*-values.

The yield surfaces predicted for the AKDQ steel and the AA5042 aluminum for the plane  $\sigma_{11}, \sigma_{22}$ , with  $\sigma_{33} = 0$ , are presented in Fig. 4a and b, respectively.

Since the AKDQ is quite isotropic, as expected the yield surfaces are very similar, and the points related with the yield stress in RD, transverse direction (TD) and the biaxial one are very close for both yield criteria. On the contrary, for the AA5042, the yield surfaces predicted by both yield criteria are completely different. Moreover, the CB2001 yield surface exhibits sharper corners, for both materials.

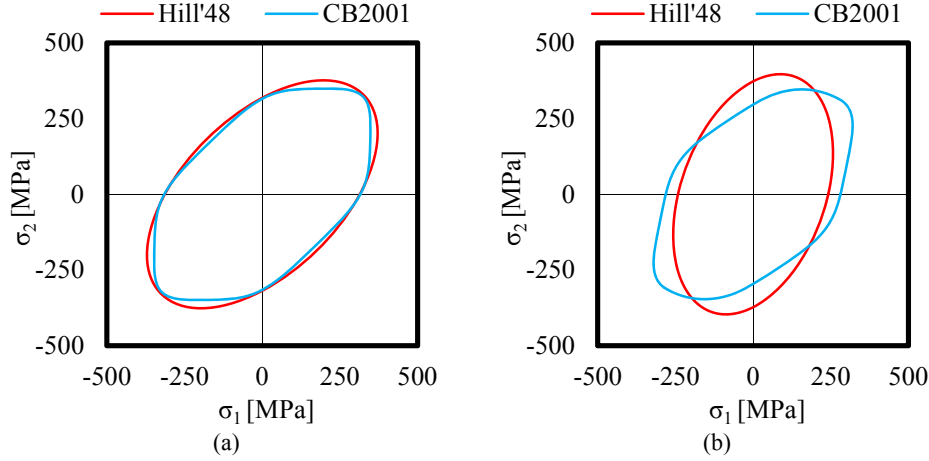


Fig. 4 – Predicted yield surfaces in the  $\sigma_{11}, \sigma_{22}$  plane for: a) AKDQ; b) AA5042.

#### 4. RESULTS AND DISCUSSION

The  $r$ -values and yield stresses directionalities (the anisotropy) are the input parameters for the phenomenological constitutive models, and are directly linked with the earing phenomenon. In fact, it has been stated that a good prediction of such material directionalities controls the overall behavior of the earing profile. Based on these results, Yoon et al. 2011 [29] proposed an analytical function to estimate the cup height directionality,

$$H^{\text{cup}}(\theta) = t_0 + r_c + \frac{R_b}{A_{\theta+90} + 1} \left( d^{A_{\theta+90}} - \frac{1}{d} \right) B_{\theta}^{A_{\theta+90}}, \quad (36)$$

where  $t_0$  is the initial blank thickness,  $R_b$  is the blank radius and  $r_c$  is the radius of the cup defined by the punch fillet radius. The  $r$ -value and the yield stress directionalities influence is dictated by

$$A_{\theta+90} = \frac{r_{\theta+90}}{1 + r_{\theta+90}} \quad \text{and} \quad B_{\theta} = \left( \frac{\sigma_{\text{ref}}}{\sigma_{\theta}^{\text{T}}} \right)^{\beta'}, \quad (37)$$



The numerical, experimental and analytical predictions of the cup height at the end of the deep drawing stage are compared in Fig. 6, for both materials. The analytical height was estimated based on the  $r$ -value and yield stress directionalities predicted using the CB2001 yield criterion, since it allows a better correlation with the experimental values (see Fig. 2 and Fig. 3). Globally, the cup height is relatively well predicted by either the analytical function or the numerical simulations. However, the number of ears and their peak-to-peak amplitude differs.

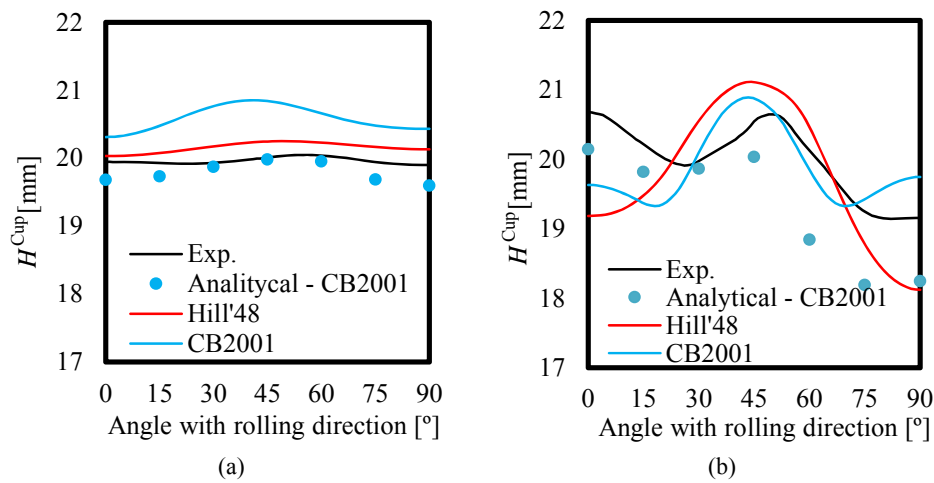


Fig. 6 – Experimental, numerical and analytical predictions of the cup height after deep drawing: a) AKDQ; b) AA5042.

In order to try to understand the differences in the predictions, the stress and strain states evolutions were analyzed for points located in the outermost flange, at every  $15^\circ$  with RD. Figure 7 presents the evolution of the ratio between the plastic strain along the radial and the thickness direction, estimated from the numerical results, and the  $r$ -values estimated with the CB2001 for each angle with RD, for both materials. The results presented correspond to the simulations performed with the CB2001, until a maximum value of the punch stroke of 20 mm, corresponding approximately to the instant at which the blank holder loses the contact with the blank. In case of AKDQ, the estimated  $\varepsilon_r/\varepsilon_t$  values are always higher than the  $r_{\theta+90}$  predicted by the CB2001. However, for the AA5042, there is a correlation between the  $\varepsilon_r/\varepsilon_t$  and the  $r_{\theta+90}$ , except for  $\theta=60^\circ$  and  $\theta=75^\circ$ . These different behaviors of the outer most flange can be explained based on the stress component

in the thickness direction, as shown in Fig. 8. For the AKDQ the blank-holder force is distributed more or less evenly in the entire flange, due to the almost isotropic behavior. Thus, for each in-plane direction, the stress component in the thickness direction is nonzero, and tends to increase with the punch displacement as a result of the decrease of the flange area. In case of AA5042, the blank-holder force is unevenly distributed, leading to null values except for  $\theta=60^\circ$ ,  $\theta=75^\circ$  and  $\theta=90^\circ$ . These results indicate the influence of nonzero stress components in the thickness direction, modifying the shear stress state assumed by Yoon et al. [29] in their analytical formulation.

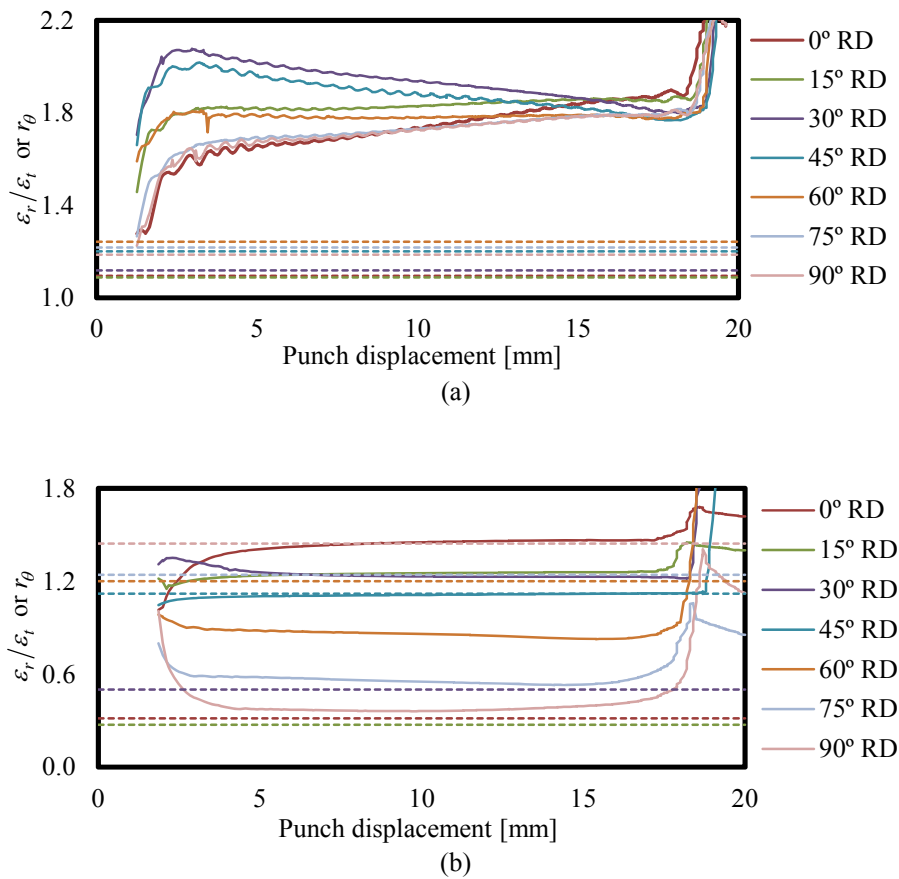


Fig. 7 – Evolution, with the punch displacement, of  $\varepsilon_r/\varepsilon_t$  and  $r$ -values estimated with the CB2001, for each angle with RD: a) AKDQ; b) AA5042.

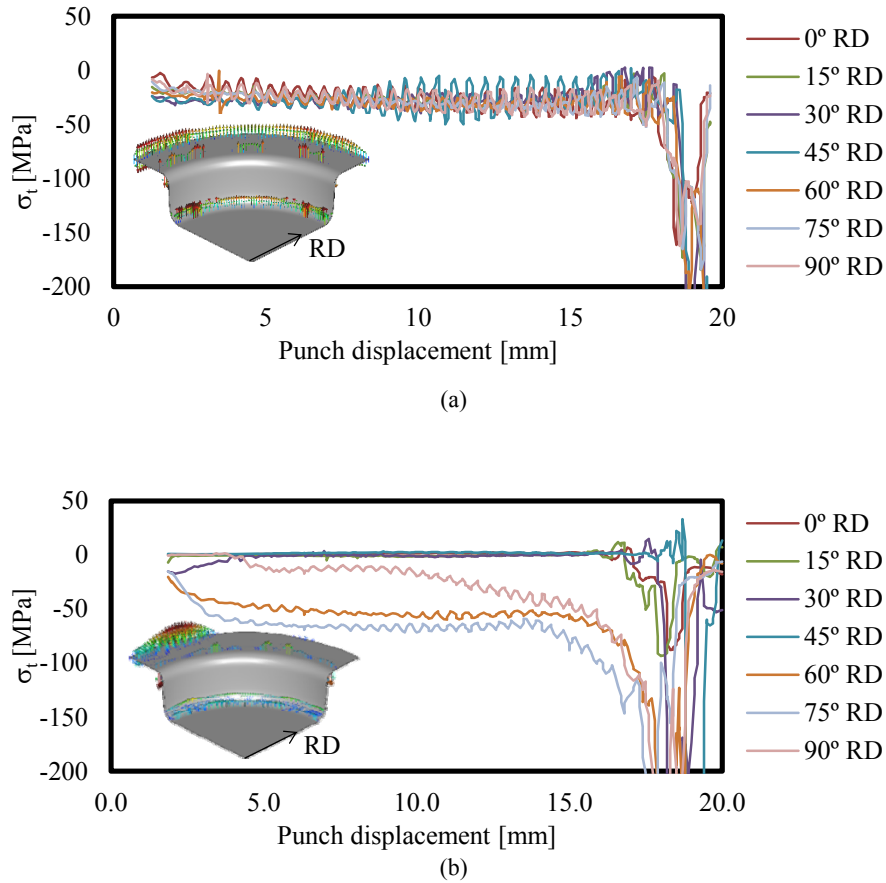
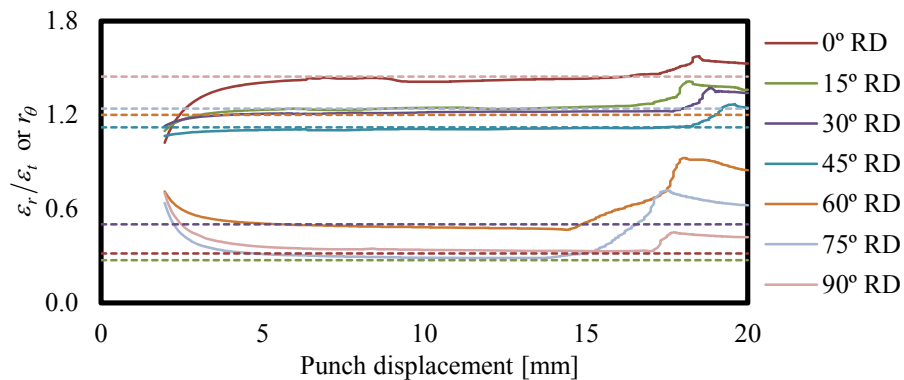


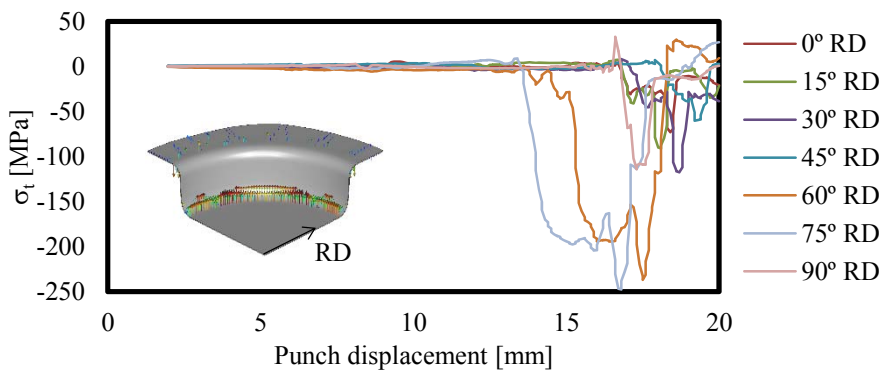
Fig. 8 – Evolution of the stress component in the thickness direction as function of the punch displacement, for several angles with RD: a) AKDQ; b) AA5042.

The numerical simulation of the deep drawing of the cylindrical cup was also performed considering a constant gap between the blank-holder and the die (0.27 mm), for the AA5042 using the CB2001. In this condition, the stress component in the thickness direction remains always close to zero for all directions, until a punch displacement of approximately 14.0 mm (see Fig. 9b). Therefore, the estimated  $\varepsilon_r/\varepsilon_t$  values are always close to the  $r_{\theta+90}$  values predicted by the CB2001, as shown in Fig. 9a. However, the stress directionalities can have more impact than the  $r$ -values in the estimative of the cup height and ears profile [29]. Therefore, Fig. 10 presents the evolution of the ratio between the circumferential stress and

the flow stress, estimated from the numerical results, and the ratio between the yield stress estimated with the CB2001 and  $Y_0$ , for each angle with RD. Also in this case the estimated  $\sigma_\theta/Y$  values are always close to the  $\sigma_{\theta+90}/Y_0$  values predicted by the CB2001, for the simulation performed with a constant gap between the blank holder and the die (see in Fig. 10b).



(a)



(b)

Fig. 9 – Numerical simulation of AA5042 considering a fixed position of the blank-holder: evolution with the punch displacement of: a)  $\varepsilon_r/\varepsilon_t$  and  $r$ -values estimated with the CB2001, for each angle with RD; b) the stress component in the thickness direction, for each angle with RD.

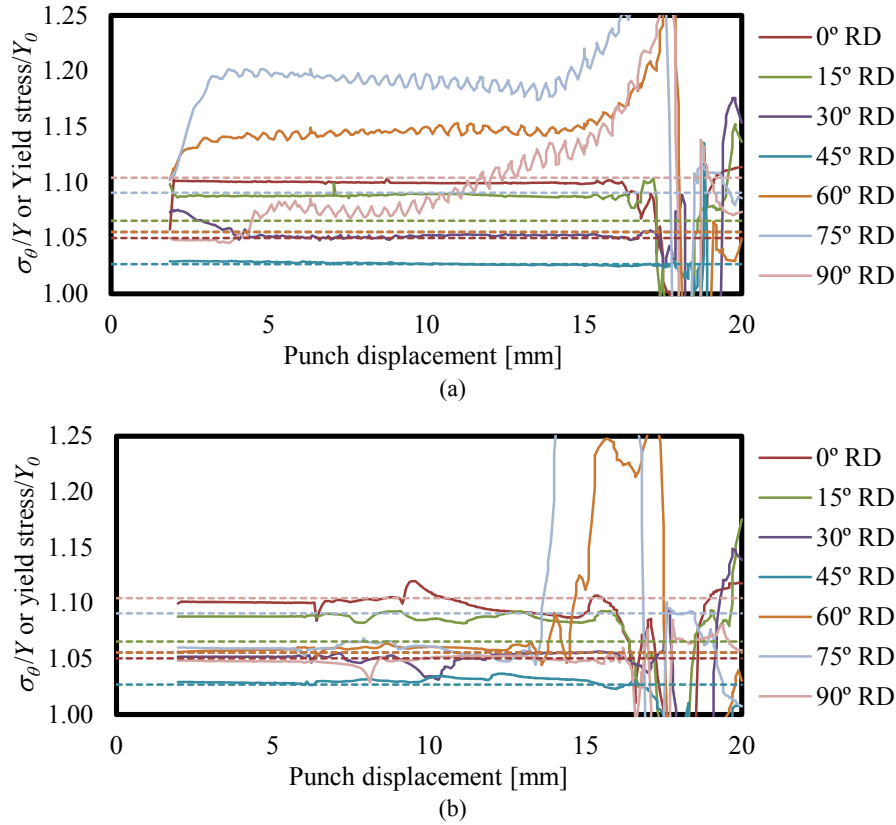


Fig. 10 – Evolution with the punch displacement of  $\sigma_\theta/Y$  and ratio between the yield stress estimated with the CB2001 and  $Y_0$ , for each angle with RD. Numerical simulation of AA5042 considering: a) a constant blank holder force; b) a fixed position of the blank-holder.

For a constant blank holder force, there is a correlation between the  $\sigma_\theta/Y$  and the  $\sigma_{\theta+90}/Y_0$ , except for  $\theta \geq 60^\circ$  (see in Fig. 10a). Consequently, the numerically predicted cup height becomes closer to the analytical one when using the fixed gap (labelled CB2001F), as shown in Fig. 11a. The comparison between both numerical results shows that the higher differences occur for  $\theta \geq 60^\circ$ , which corresponds to zone of the flange with compressive stresses in the thickness direction (see Fig. 8b. Yoon and Cazacu [32] reported a similar trend with the friction coefficient change, i.e. the decrease of this value lead to a smaller cup height mainly for  $\theta \geq 60^\circ$ . The same was observed for the simulation performed with a null value for the friction coefficient (labelled CB2001(f = 0)), as also shown in Fig. 11a. Although not shown here, the stress component in the thickness

direction vanishes, in the most outer flange, for  $\theta = 90^\circ$ , when using a null friction coefficient. Both results highlight the importance of the stress state in the cup's flange for an accurate description of the cup height, number and amplitude of the ears. The analysis of Fig. 6b and Fig. 11a indicates that the value predicted for the peak-to-peak amplitude of the cup height is closer for the numerical results obtained with a constant blank-holder force with the Hill'48 yield criterion and a fixed blank-holder with the CB2001, than with both conditions using the CB2001 yield criterion. This is also related with the stress state in the flange, since the Hill'48 predicts a higher blank thickening in the flange area leading to a maximum value of the gap between the blank-holder and the die similar to the one imposed in the simulation performed with a fixed value (see Fig. 11b). For the AKDQ steel the friction coefficient does not change the earing trend and only slightly changes the cup height, as shown in Fig. 12a, for a friction coefficient of zero (labelled CB2001( $f = 0$ )) and 0.1 (labelled CB2001( $f = 0.1$ )). This is related with the small change in the blank-holder displacement (see Fig. 12b), influenced by the small increase of the radial stress, induced by the increase of the friction coefficient. Nevertheless, this effect is similar for the entire flange, leading to a negligible effect in the earing trend. Thus, a good prediction of the material directionalities controls the overall accuracy of the earing profile, because it dictates the interaction with process parameters such as the blank holder force distribution.

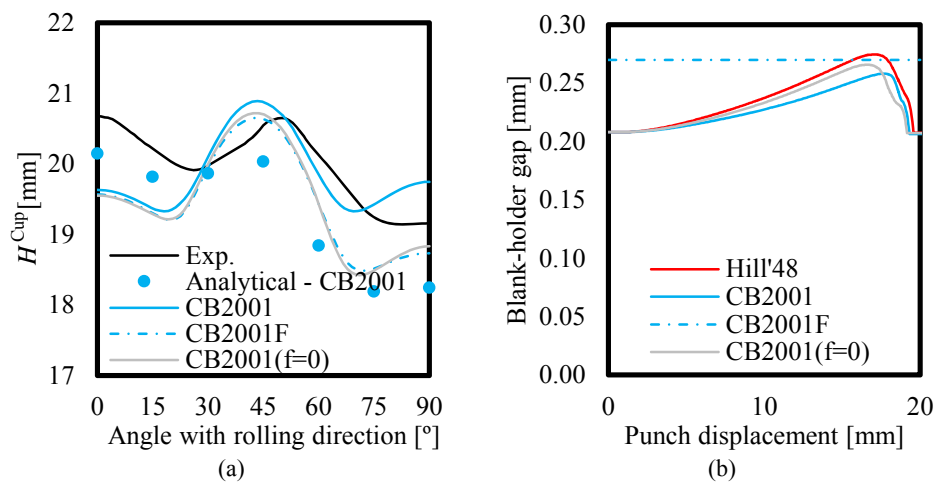


Fig. 11 – a) Experimental, numerical and analytical predictions of the AA5042 cup height after deep drawing; b) evolution with the punch displacement of the blank holder gap with the die.

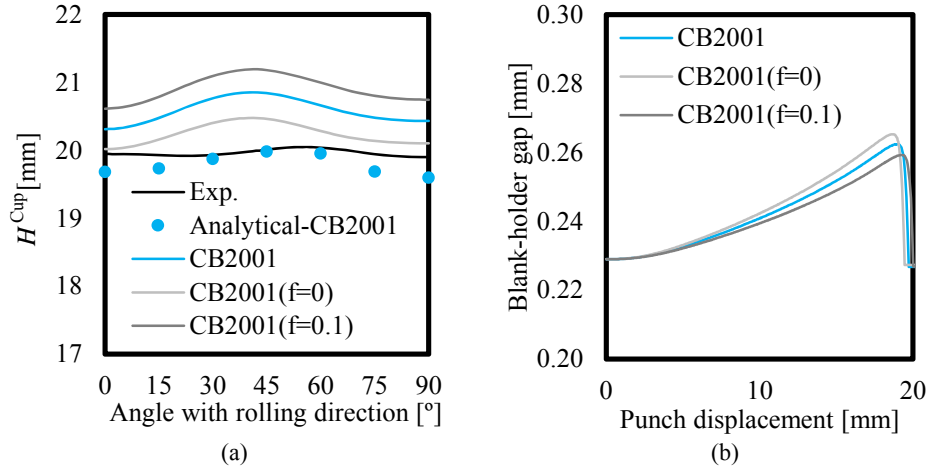


Fig. 12 – a) Experimental, numerical and analytical predictions of the AKDQ cup height after deep drawing; b) evolution with the punch displacement of the blank holder gap with the die.

The computational efficiency of the proposed integration algorithm is shown in Table 3, by means of both elapsed real time and total number of time increments to carry out the simulation of the deep drawing phase, using the two yield criteria, i.e. Hill48 and CB2001. The number of increments with its size reduced (*N<sub>Trial</sub>* Strategy), caused by convergence problems during the iterative loop, was selected in this study to indicate the robustness of the integration algorithm. Indeed, the so-called *N<sub>Trial</sub>* strategy, currently implemented in DD3IMP, allows overcoming most of convergence issues by automatically reducing the increment size, when convergence is not attained within the allowed number of iterations. The results show that the computational efficiency is not directly penalized by the selection of the CB2001 yield criterion. In fact, the numerical simulations performed with AKDQ steel, presenting a more isotropic behavior, tends to require more iterations. This is mainly related with the difficulties associated with contact status convergence for a higher number of nodes, in each iteration. This effect is more visible for AKDQ due to the alignment of the nodes along the circumferential direction, enabling the simultaneous change of the contact conditions that results in higher oscillations of the contact forces and, consequently, of the non-equilibrated forces and stress fields (see Fig. 8).

Nevertheless, during the deep drawing phase, only small differences in the punch force evolution predicted with both yield criteria can be observed. These results are shown in Fig. 13a and Fig. 14a, for the AKDQ and the AA5042, respectively. For AKDQ, the higher thickening predicted for the outermost flange, for a punch displacement of 35 mm (see Fig. 13b), results in a slightly higher value for the maximum punch force, visible also for the ironing stage. In case of

AA5042, the maximum value of the punch force is always slightly higher when using CB2001. However, it is more difficult to correlate this result with the thickening predicted for the most outer flange, for a punch displacement of 35 mm (see Fig. 14b). As expected the ironing process increases the cup height, although not changing the peak-to-peak amplitude, for both yield criteria. The results for the cup height at the end of the ironing stage are shown in Fig. 15 for both materials. They should be compared with the ones presented in Fig. 6 to confirm that also the experimental results show a similar profile before and after the ironing stage. Globally, the conditions for the ironing phase are quite different for both materials, since the blanks present distinct thickness profiles at the end of the drawing stage and similar at the end of the ironing (see Fig. 1). Moreover, conditions differ for both yield criteria, since the deep drawing stage imposes cups with different heights and maximum thickness values. Therefore, the analysis of the computational performance based on the number of increments for the ironing stage is biased.

Table 3

Computational performance of the deep drawing stage using different yield criteria

	AKDQ		AA5042	
	Hill'48	CB2001	Hill'48	CB2001
N° of increments	553	667	553	512
N° of iterations	5727	5853	5298	4075
$N_{Trial}$ strategy	73	226	137	78
Computational time [hours]	5.35	5.96	4.34	3.35

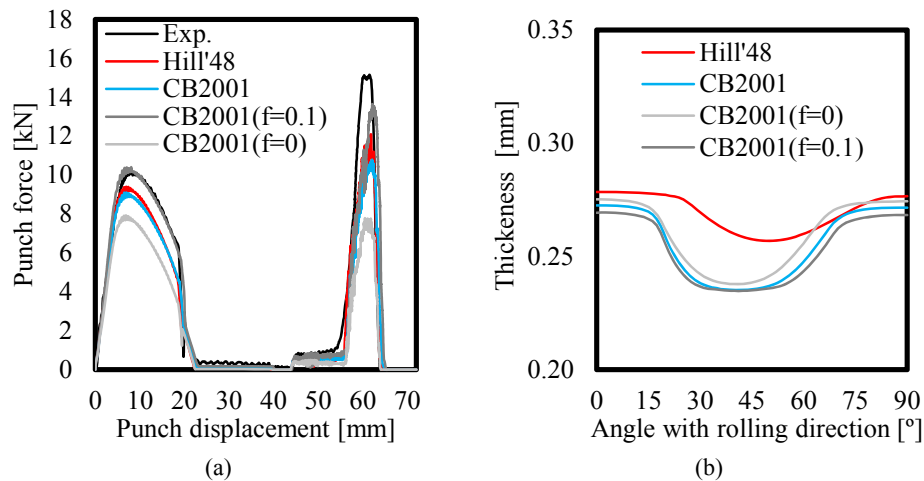


Fig. 13 – AKDQ: a) punch force evolution with its displacement; b) thickness distribution on the most outer flange, for a punch displacement of 35 mm.

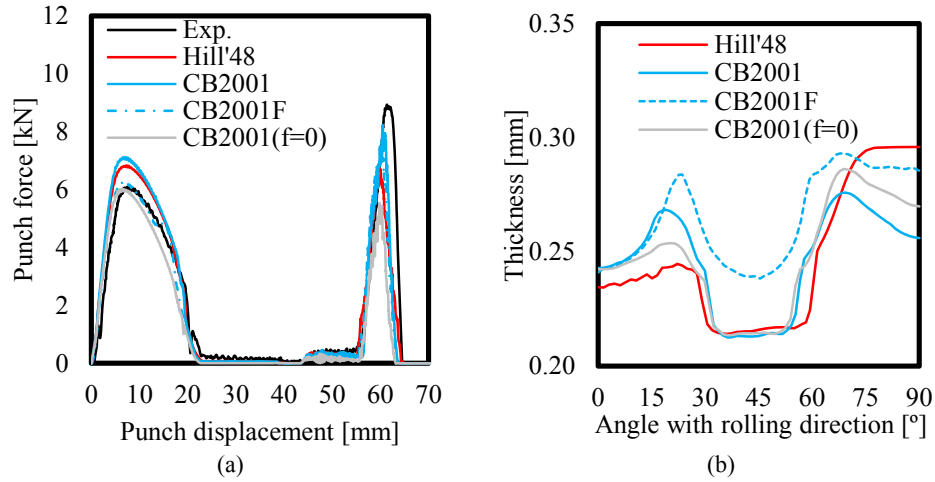


Fig. 14 – AA5042: a) Punch force evolution with its displacement; b) thickness distribution on the most outer flange, for a punch displacement of 35 mm.

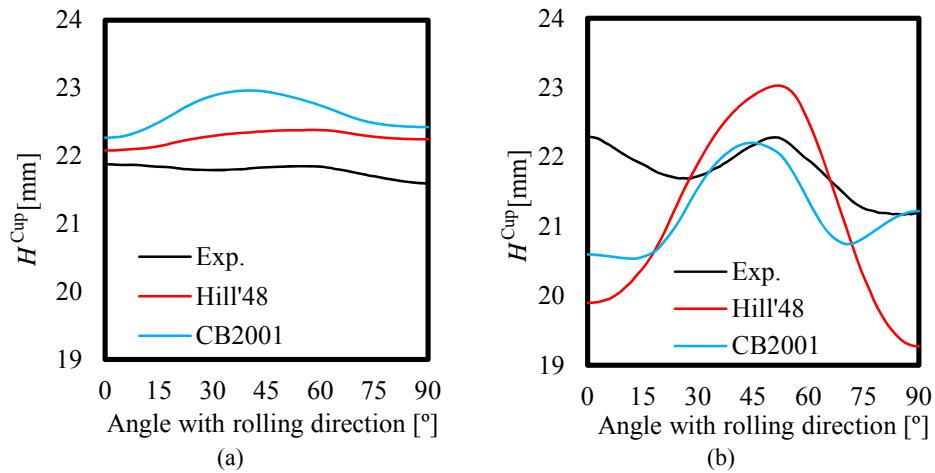


Fig. 15 – Experimental and numerical predictions of the cup height after the ironing process for: a) AKDQ; b) AA5042.

## 5. CONCLUDING REMARKS

The numerical simulation of the deep drawing of a cylindrical cup is performed with the implicit in-house finite element solver DD3IMP. The analysis is focused in the accurate description of the orthotropic behavior of metallic sheets

using the non-quadratic anisotropic yield criterion CB2001. Two different materials are considered for the blank: AA5042 aluminum alloy and AKDQ steel. The material parameters are identified from experimental data, by best fit to the experimental results of conventional uniaxial tensile tests, biaxial yield stress and  $r_b$ . The results shown that the accuracy of the earing profile prediction is strongly influenced by the description of the anisotropy of both  $r$ -values and yield stresses. Additionally, for materials with a strong anisotropic behavior of the  $r$ -values (e.g. AA5042 aluminum alloy), the earing profile is influenced by the global process modeling, particularly the contact conditions in the flange. This is related with the uneven thickness strain distribution in the sheet plane, which leads to a non-uniform contact force distribution, more concentrated in a limited region of the flange. Also, the computational time of the numerical simulations is mainly dictated by the contact conditions between the die and the blank-holder, with a negligible influence of the sharper curvature of the yield surface. Thus, when using analytical partial derivatives of the yield surface in the constitutive model numerical integration, the use of non-quadratic anisotropic yield criteria does not affect the computational performance efficiency.

#### APPENDIX A: ANALYTICAL EXPRESSIONS OF THE DERIVATIVES OF THE CB2001 YIELD CRITERION

This section is related to the calculations of the following quantities,

$$\beta, \quad \mathbf{V} = \frac{\partial \bar{\sigma}}{\partial (\boldsymbol{\sigma}'_F - \mathbf{X}_F)}, \quad \mathbf{Q} = \frac{\partial^2 \bar{\sigma}}{\partial (\boldsymbol{\sigma}'_F - \mathbf{X}_F)^2}. \quad (40)$$

specifically related with the numerical implementation of the CB2001 yield criterion in the FE solver DD3IMP.

Taking into account the isochoric character of plasticity, the implementation of the state update algorithm in DD3IMP is done in a five-dimensional deviatoric space, instead of the Cartesian space, given that any symmetric deviatoric tensor has only 5 independent components [23]. Thus, considering the effective deviatoric stress state tensor  $\Sigma_{ij}$ ,  $i, j = 1, 2, 3$ , represented in the Cartesian space, its components in the five-dimensional deviatoric space  $\Sigma_I$ ,  $I = 1, \dots, 5$ , are given by the following transformations

$$\Sigma_1 = \frac{1}{\sqrt{2}}(\Sigma_{11} - \Sigma_{22}); \quad \Sigma_2 = \sqrt{\frac{3}{2}}(\Sigma_{11} + \Sigma_{22}) = -\sqrt{\frac{3}{2}}\Sigma_{33};$$
(41)

$$\Sigma_3 = \sqrt{2}\Sigma_{23}; \quad \Sigma_4 = \sqrt{2}\Sigma_{13}; \quad \Sigma_5 = \sqrt{2}\Sigma_{12}.$$

This transformation from  $\Sigma_{ij}$  ( $i, j = 1, 2, 3$ ) to  $\Sigma_I$  (with  $I = 1, \dots, 5$ ) can also be written in matrix form using Voigt notation of the symmetric tensor  $\Sigma_{ij}$  ( $i, j = 1, 2, 3$ ), introducing the following transformation matrix:

$$\begin{Bmatrix} \Sigma_1 \\ \Sigma_2 \\ \Sigma_3 \\ \Sigma_4 \\ \Sigma_5 \end{Bmatrix} = \begin{bmatrix} 1/\sqrt{2} & -1/\sqrt{2} & 0 & 0 & 0 & 0 \\ \sqrt{3/2} & \sqrt{3/2} & 0 & 0 & 0 & 0 \\ 0 & 0 & 0 & \sqrt{2} & 0 & 0 \\ 0 & 0 & 0 & 0 & \sqrt{2} & 0 \\ 0 & 0 & 0 & 0 & 0 & \sqrt{2} \end{bmatrix} \begin{Bmatrix} \Sigma_{11} \\ \Sigma_{22} \\ \Sigma_{33} \\ \Sigma_{23} \\ \Sigma_{13} \\ \Sigma_{12} \end{Bmatrix}. \quad (42)$$

The inverse transformation, from the five-dimensional space to the Cartesian one, i.e. from  $\Sigma_I$  (with  $I = 1, \dots, 5$ ) to  $\Sigma_{ij}$  ( $i, j = 1, 2, 3$ ), can also be written as:

$$\begin{Bmatrix} \Sigma_{11} \\ \Sigma_{22} \\ \Sigma_{33} \\ \Sigma_{23} \\ \Sigma_{13} \\ \Sigma_{12} \end{Bmatrix} = \begin{bmatrix} 1/\sqrt{2} & 1/\sqrt{6} & 0 & 0 & 0 & 0 \\ -1/\sqrt{2} & 1/\sqrt{6} & 0 & 0 & 0 & 0 \\ 0 & -\sqrt{2/3} & 0 & 0 & 0 & 0 \\ 0 & 0 & 1/\sqrt{2} & 0 & 0 & 0 \\ 0 & 0 & 0 & 1/\sqrt{2} & 0 & 0 \\ 0 & 0 & 0 & 0 & 1/\sqrt{2} & 0 \end{bmatrix} \begin{Bmatrix} \Sigma_1 \\ \Sigma_2 \\ \Sigma_3 \\ \Sigma_4 \\ \Sigma_5 \end{Bmatrix}. \quad (43)$$

The same can also be applied for any fourth-order symmetric and deviatoric tensor  $\mathbf{T}$ , which corresponds to  $T_{KL}$  (with  $K, L = 1, \dots, 6$ ) using the Voigt notation. Thus, the use of the five-dimensional deviatoric space enables expressing this tensorial quantity as  $T_{IJ}$  (with  $I, J = 1, \dots, 5$ ). This reduces the number of independent terms and simplifies the notation, as shown afterwards, for the second-order tensor  $\mathbf{V}$  and particularly for the fourth-order tensor  $\mathbf{Q}$ .

In the case of CB2001 yield criterion, the equivalent stress is given by Eq. 28, but the invariants  $J_2^0$  and  $J_3^0$  can be written as a function of the components of the effective stress tensor in the five-dimensional deviatoric space, i.e.

$$J_2^0 = A_1 \Sigma_1^2 + A_2 \Sigma_2^2 + A_3 \Sigma_1 \Sigma_2 + A_4 \Sigma_5^2 + A_5 \Sigma_4^2 + A_6 \Sigma_3^2 \quad \text{and} \quad (44)$$

$$J_3^0 = B_1 \Sigma_1^3 + B_2 \Sigma_1^2 \Sigma_2 + B_3 \Sigma_1 \Sigma_2^2 + B_4 \Sigma_2^3 + B_5 \Sigma_1 \Sigma_3^2 + B_6 \Sigma_2 \Sigma_3^2 + B_7 \Sigma_1 \Sigma_4^2 + B_8 \Sigma_2 \Sigma_4^2 + B_9 \Sigma_1 \Sigma_5^2 + B_{10} \Sigma_2 \Sigma_5^2 + B_{11} \Sigma_3 \Sigma_4 \Sigma_5, \quad (45)$$

where

$$\begin{aligned} A_1 &= 1/12(4a_1 + a_2 + a_3) & B_1 &= 1/(54\sqrt{2})(4b_1 + b_2 + b_3 - 4b_4) \\ A_2 &= 1/4(a_2 + a_3) & B_2 &= 3/(\sqrt{3})/(54\sqrt{2})(2b_1 + b_2 + b_3 + 2b_4) \\ A_3 &= 1/2\sqrt{3}(a_3 - a_2) & B_3 &= 9/(54\sqrt{2})(b_2 - b_3) \\ A_4 &= 1/2(a_4) & B_4 &= 3/(\sqrt{3})/(54\sqrt{2})(-2b_1 + b_2 + b_3 - 2b_4) \\ A_5 &= 1/2(a_5) & B_5 &= -\sqrt{2}/12(2b_6 + b_7) \\ A_6 &= 1/2(a_6) & B_6 &= -\sqrt{6}/12(b_7) \\ & & B_7 &= -\sqrt{2}/12(b_8 - 4b_9) \\ & & B_8 &= -\sqrt{6}/12(b_8) \\ & & B_9 &= -\sqrt{2}/6(b_5 - b_{10}) \\ & & B_{10} &= \sqrt{6}/6(b_{10}) \\ & & B_{11} &= 1/\sqrt{2}(b_{11}) \end{aligned} \quad (46)$$

The scalar  $\beta$  has to be evaluated whenever the effective stress state at the beginning of the time increment is elastic. It is determined with the consistency condition, such that

$$\mathcal{F}(\beta) = \bar{\sigma}(\boldsymbol{\sigma}_0 - \mathbf{X}_0, \Delta \boldsymbol{\varepsilon}', \beta) - Y_I = \bar{\sigma}(\Sigma_0, \Delta \boldsymbol{\varepsilon}', \beta) - Y_I = 0, \quad (47)$$

where subscript  $I$  denotes the flow stress at the beginning of the time increment.  $\beta$  is the only unknown of this non-linear equation. Thus, the Newton method is used to iteratively determine  $\beta$ , given by the relation

$$\beta^{i+1} = \beta^i - \frac{\mathcal{F}^i}{\mathcal{F}^{i'}}. \quad (48)$$

The scalar quantities  $\mathcal{F}^i$  and  $\mathcal{F}^{i'}$  are required, being the first one given by Eq. 47 and the second one by

$$\mathcal{F}^{i'} = \frac{\partial \bar{\sigma}(\boldsymbol{\sigma}_0 - \mathbf{X}_0, \Delta \boldsymbol{\varepsilon}', \beta)}{\partial \beta^i} = \frac{\partial \bar{\sigma}}{\partial \boldsymbol{\Sigma}^i} \frac{\partial \boldsymbol{\Sigma}^i}{\partial \beta^i} = \mathbf{V}^i : (2\mu \Delta \boldsymbol{\varepsilon}'). \quad (49)$$

Taking into account the equivalent stress definition given in Eq. 28 and the two generalized invariants defined in the five-dimensional deviatoric space, after some mathematical developments the tensor  $\mathbf{V}$  can be written as

$$V_I|_{CB2001} = \frac{\partial \bar{\sigma}}{\partial \Sigma_I} = \frac{9}{2\bar{\sigma}^5} \left[ 3(J_2^0)^2 \frac{\partial J_2^0}{\partial \Sigma_I} - 2c(J_3^0) \frac{\partial J_3^0}{\partial \Sigma_I} \right], \text{ with } I = 1, \dots, 5. \quad (50)$$

The tensor  $\mathbf{Q}$  is given by

$$\begin{aligned} Q_{IJ}|_{CB2001} &= \frac{\partial^2 \bar{\sigma}}{\partial \Sigma_I \partial \Sigma_J} = \frac{\partial V_I}{\partial \Sigma_J} = \\ &= -\frac{5}{\bar{\sigma}} V_I V_J + \frac{9}{2\bar{\sigma}^5} \left[ 6(J_2^0) \frac{\partial J_2^0}{\partial \Sigma_I} \cdot \frac{\partial J_2^0}{\partial \Sigma_J} + 3(J_2^0)^2 \frac{\partial^2 J_2^0}{\partial \Sigma_I \partial \Sigma_J}, \right. \\ &\quad \left. - 2c(J_3^0) \frac{\partial J_3^0}{\partial \Sigma_I} \cdot \frac{\partial J_3^0}{\partial \Sigma_J} - 2c(J_3^0) \frac{\partial^2 J_3^0}{\partial \Sigma_I \partial \Sigma_J} \right] \end{aligned} \quad (51)$$

with  $I, J = 1, \dots, 5$ . The terms relative to the first order derivatives  $\frac{\partial J_2^0}{\partial \Sigma_I}$  and  $\frac{\partial J_3^0}{\partial \Sigma_I}$  are defined as

$$\frac{\partial J_2^0}{\partial \Sigma_I} = \begin{Bmatrix} 2A_1 \Sigma_1 + A_3 \Sigma_2 \\ 2A_2 \Sigma_2 + A_3 \Sigma_1 \\ 2A_6 \Sigma_3 \\ 2A_5 \Sigma_4 \\ 2A_4 \Sigma_5 \end{Bmatrix}, \quad (52)$$

and

$$\frac{\partial J_3^0}{\partial \Sigma_I} = \begin{Bmatrix} 3B_1 \Sigma_1^2 + 2B_2 \Sigma_1 \Sigma_2 + B_3 \Sigma_2^2 + B_5 \Sigma_3^2 + B_7 \Sigma_4^2 + B_9 \Sigma_5^2 \\ B_2 \Sigma_1^2 + 2B_3 \Sigma_1 \Sigma_2 + B_4 \Sigma_2^2 + B_6 \Sigma_3^2 + B_8 \Sigma_4^2 + B_{10} \Sigma_5^2 \\ 2B_5 \Sigma_1 \Sigma_3 + 2B_6 \Sigma_2 \Sigma_3 + B_{11} \Sigma_4 \Sigma_5 \\ 2B_7 \Sigma_1 \Sigma_4 + 2B_8 \Sigma_2 \Sigma_4 + B_{11} \Sigma_3 \Sigma_5 \\ 2B_9 \Sigma_1 \Sigma_5 + 2B_{10} \Sigma_2 \Sigma_5 + B_{11} \Sigma_3 \Sigma_4 \end{Bmatrix}, \quad (53)$$

with  $I = 1, \dots, 5$ . The terms relative to the second order derivatives,  $\frac{\partial^2 J_2^0}{\partial \Sigma_I \partial \Sigma_J}$  and

$\frac{\partial^2 J_3^0}{\partial \Sigma_I \partial \Sigma_J}$ , are defined as

$$\frac{\partial^2 J_2^0}{\partial \Sigma_I \partial \Sigma_J} = \begin{Bmatrix} 2A_1 & A_3 & 0 & 0 & 0 \\ A_3 & 2A_2 & 0 & 0 & 0 \\ 0 & 0 & 2A_6 & 0 & 0 \\ 0 & 0 & 0 & 2A_5 & 0 \\ 0 & 0 & 0 & 0 & 2A_4 \end{Bmatrix}, \quad (54)$$

and

$$\frac{\partial^2 J_3^0}{\partial \Sigma_I \partial \Sigma_J} = \begin{Bmatrix} 6B_1 \Sigma_1 + 2B_2 \Sigma_2 & 2B_2 \Sigma_1 + 2B_3 \Sigma_2 & 2B_5 \Sigma_3 & 2B_7 \Sigma_4 & 2B_9 \Sigma_5 \\ 2B_2 \Sigma_1 + 2B_3 \Sigma_2 & 2B_3 \Sigma_1 + 2B_4 \Sigma_2 & 2B_6 \Sigma_3 & 2B_8 \Sigma_4 & B_{10} \Sigma_5 \\ 2B_5 \Sigma_3 & 2B_6 \Sigma_3 & 2B_5 \Sigma_1 + 2B_6 \Sigma_2 & B_{11} \Sigma_5 & B_{11} \Sigma_4 \\ 2B_7 \Sigma_4 & 2B_8 \Sigma_4 & B_{11} \Sigma_5 & 2B_7 \Sigma_1 + 2B_8 \Sigma_2 & B_{11} \Sigma_3 \\ 2B_9 \Sigma_5 & 2B_{10} \Sigma_5 & B_{11} \Sigma_4 & B_{11} \Sigma_3 & 2B_9 \Sigma_1 + 2B_{10} \Sigma_2 \end{Bmatrix} \quad (55)$$

The initial effective stress state is then updated to the initial yield surface as

$$(\boldsymbol{\sigma}_0 - \mathbf{X}_0)^* \leftarrow \boldsymbol{\sigma}_0 - \mathbf{X}_0 + \beta(2\mu\Delta\boldsymbol{\varepsilon}'). \quad (56)$$

**Acknowledgements.** The authors gratefully acknowledge the financial support of the Portuguese Foundation for Science and Technology (FCT) under project PTDC/EMS-TEC/1805/2012. P.D. Barros is also grateful to the FCT for the PhD Grant SFRH/BD/98545/2013 and D.M. Neto is also grateful for the Post-Doctoral Fellowship SFRH/BPD/101334/2014.

*Received on June 8, 2015*

## REFERENCES

1. GANTAR, G., PEPELNJAK, T., KUZMAN, K., *Optimization of sheet metal forming processes by the use of numerical simulations*, J. Mater. Process. Technol., **130–131**, pp. 54–59, 2002.
2. NOELS, L., STAINIER, L., PONTHOT, J-P., *Combined implicit/explicit time-integration algorithms for the numerical simulation of sheet metal forming*, J. Comput. Appl. Math., **168**, pp. 331–339, 2004.
3. YANG, D.Y., JUNG, D.W., SONG, I.S., YOO, D.J., LEE, J.H., *Comparative investigation into implicit, explicit, and iterative implicit/explicit schemes for the simulation of sheet-metal forming processes*, J. Mater. Process. Technol., **50**, pp. 39–53, 1995.
4. TEKKAYA, A.E., MARTINS, P.A.F., *Accuracy, reliability and validity of finite element analysis in metal forming: a user's perspective*, Engineering Computations, **26**, 8, pp. 1026–1055, 2009.
5. SAFAEI, M., *Constitutive modelling of anisotropic sheet metals based on a non-associated flow rule*, PhD Thesis, Faculty of Engineering and Architecture, Ghent University, Belgium, 2013.
6. NETO, D.M., OLIVEIRA, M.C., ALVES, J.L., MENEZES, L.F., *Influence of the plastic anisotropy modelling in the reverse deep drawing process simulation*, Mater Des, **60**, pp. 368–379, 2014.
7. CAZACU, O., BARLAT, F., *Generalization of Drucker's Yield Criterion to Orthotropy*, Math. Mech. Solids., **6**, 6, pp. 613–630, 2001.
8. MENEZES, L.F., TEODOSIU, C., *Three-dimensional numerical simulation of the deep-drawing process using solid finite elements*, J. Mater. Process. Technol., **97**, pp. 100–106, 2000.
9. OLIVEIRA, M.C., ALVES, J.L., MENEZES, L.F., *Algorithms and Strategies for Treatment of Large Deformation Frictional Contact in the Numerical Simulation of Deep Drawing Process*, Arch. Comput. Methods. Eng., **15**, pp. 113–162, 2008.
10. ALART, P., CURNIER, A., *A mixed formulation for frictional contact problems prone to Newton like solution methods*, Comput. Methods. Appl. Mech. Eng., **92**, 3, pp. 353–375, 1991.

11. YAMADA, Y., YOSHIMURA, N., SAKURAI, T., *Plastic stress-strain matrix and its application for the solution of elastic-plastic problems by the finite element method*, Int J Mech Sci, **10**, 5, pp. 343–354, 1968.
12. NETO, D.M., OLIVEIRA, M.C., MENEZES, L.F., ALVES, J.L., *Applying Nagata patches to smooth discretized surfaces used in 3D frictional contact problems*, Comput. Methods. Appl. Mech. Eng., **271**, pp. 296–320, 2014.
13. NETO, D.M., OLIVEIRA, M.C., MENEZES, L.F., ALVES, J.L., *Nagata patch interpolation using surface normal vectors evaluated from the IGES file*, Finite Elem Anal Des, **72**, pp. 35–46, 2013.
14. TEODOSIU, C., DANIEL, D., CAO, H-L., DUVAL, J-L., *Modelling and simulation of the can-making process using solid finite elements*, J. Mater. Process. Technol., **50**, pp. 133–143, 1995.
15. MENEZES, L.F., NETO, D.M., OLIVEIRA, M.C., ALVES, J.L., *Improving Computational Performance through HPC Techniques: case study using DD3IMP in-house code*, AIP Conf. Proc, **1353**, pp. 1220–1225, 2011.
16. HILL, R., *A Theory of the Yielding and Plastic Flow of Anisotropic Metals*, Proc. R. Soc. A. Math. Phys. Eng. Sci., **193**, pp. 281–297, 1948.
17. BARLAT, F., LEGE, D.J., BREM, J.C., *A six-component yield function for anisotropic materials*, Int. J. Plast., **7**, 7, pp. 693–712, 1991.
18. DRUCKER, D.C., PRAGER, W., *Soil mechanics and plastic analysis for limit design*, Q. Appl. Math., **10**, pp. 157–165, 1952.
19. KARAFILLIS, A.P., BOYCE, M.C., *A general anisotropic yield criterion using bounds and a transformation weighting tensor*, J. Mech. Phys. Solids., **41**, 12, pp. 1859–1886, 1993.
20. CAZACU, O., PLUNKETT, B., BARLAT, F., *Orthotropic yield criterion for hexagonal closed packed metals*, Int. J. Plast., **22**, 7, pp. 1171–1194, 2006.
21. LEMAITRE, J., CHABOCHE, J-L., *Mechanics of Solid Materials*, Cambridge University Press, 1990.
22. TEODOSIU, C., HU, Z., *Evolution of the intergranular microstructure at moderate and large strains: Modelling and computational significance*, Numiform'95 on Simulation of Materials Processing: Theory, Methods and Applications, Balkema, pp. 173–182, 1995.
23. ALVES, J.L., *Simulação numérica do processo de estampagem de chapas metálicas: modelação mecânica e métodos numéricos*, PhD Thesis, University of Minho, Portugal, 2003.
24. DICK, R.E., YOON, J.W., HUH, H.S., BAE, G., *BMI – Earing Evolution During Drawing and Ironing processes, Part C Benchmark Problems and Results*, Numisheet'2001 8<sup>th</sup> Int. Conf. Work. Numer. Simul. 3D Sheet Met. Form. Process, pp. 171–226, 2011.
25. HUGHES, T.J.R., *Generalization of selective integration procedures to anisotropic and nonlinear media*, Int. J. Numer. Methods. Eng., **15**, 9, pp. 1413–1418, 1980.
26. BARROS, P.D., ALVES, J.L., OLIVEIRA, M.C., MENEZES, L.F., *Earing evolution during drawing and ironing processes*, WCCM 10<sup>th</sup> World Congr. Comput. Mech., Sao Paulo, pp. 3954–3973, 2012.
27. ALVES, J.L., OLIVEIRA, M.C., MENEZES, L.F., *An advanced constitutive model in the sheet metal forming simulation: the Teodosiu microstructural model and the Cazacu Barlat yield criterion*, AIP Conf. Proc, **712**, pp. 1645–1650, 2004.
28. BANABIC, D., ARETZ, H., COMSA, D.S., PARAIANU, L., *An improved analytical description of orthotropy in metallic sheets*, Int J Plast, **21**, 3, pp. 493–512, 2005.

29. YOON, J.W., DICK, R.E., BARLAT, F., *A new analytical theory for earing generated from anisotropic plasticity*, Int J Plast, **27**, 8, pp. 1165–1184, 2011.
30. SOARE, S., YOON, J.W., CAZACU, O., *On the use of homogeneous polynomials to develop anisotropic yield functions with applications to sheet forming*, Int. J. Plast., **24**, 6, pp. 915–944, 2008.
31. BARROS, P.D., OLIVEIRA, M.C., ALVES, J.L., MENEZES, L.F., *Earing Prediction in Drawing and Ironing Processes Using an Advanced Yield Criterion*, Key Eng. Mater, **554-557**, pp. 2266–2276, 2013.
32. YOON, J.H., CAZACU, O., *Anisotropic yield function capable of predicting eight ears*, Numisheet'2001 8<sup>th</sup> Int. Conf. Work. Numer. Simul. 3D Sheet Met. Form. Process., 2011, pp. 86–91.